



Article

Transport Properties and High Temperature Raman Features of Heavily Gd-Doped Ceria

Cristina Artini ^{1,2}, Sabrina Presto ^{3,*} , Sara Massardo ¹, Marcella Pani ^{1,4},
Maria Maddalena Carnasciali ^{1,5} and Massimo Viviani ³ 

¹ Department of Chemistry and Industrial Chemistry, University of Genova, Via Dodecaneso 31, 16146 Genova, Italy; artini@chimica.unige.it (C.A.); s.massardo93@gmail.com (S.M.); marcella@chimica.unige.it (M.P.); marilena@chimica.unige.it (M.M.C.)

² Institute of Condensed Matter Chemistry and Technologies for Energy, National Research Council, CNR-ICMATE, Via De Marini 6, 16149 Genova, Italy

³ Institute of Condensed Matter Chemistry and Technologies for Energy, National Research Council, CNR-ICMATE, c/o DICCA-UNIGE, Via all'Opera Pia 15, 16145 Genova, Italy; massimo.viviani@ge.icmate.cnr.it

⁴ CNR-SPIN, Corso Perrone 24, 16152 Genova, Italy

⁵ INSTM, Genova Research Unit, Via Dodecaneso 31, 16146 Genova, Italy

* Correspondence: sabrina.presto@ge.icmate.cnr.it; Tel.: +39-010-353-6025

Received: 1 October 2019; Accepted: 29 October 2019; Published: 30 October 2019



Abstract: Transport and structural properties of heavily doped ceria can reveal subtle details of the interplay between conductivity and defects aggregation in this material, widely studied as solid electrolyte in solid oxide fuel cells. The ionic conductivity of heavily Gd-doped ceria samples ($\text{Ce}_{1-x}\text{Gd}_x\text{O}_{2-x/2}$ with x ranging between 0.31 and 0.49) was investigated by impedance spectroscopy in the 600–1000 K temperature range. A slope change was found in the Arrhenius plot at ~ 723 K for samples with $x = 0.31$ and 0.34 , namely close to the compositional boundary of the CeO_2 -based solid solution. The described discontinuity, giving rise to two different activation energies, points at the existence of a threshold temperature, below which oxygen vacancies are blocked, and above which they become free to move through the lattice. This conclusion is well supported by Raman spectroscopy, due to the discontinuity revealed in the Raman shift trend versus temperature of the signal related to defects aggregates which hinder the vacancies movement. This evidence, observable in samples with $x = 0.31$ and 0.34 above ~ 750 K, accounts for a weakening of Gd–O bonds within blocking microdomains, which is compatible with the existence of a lower activation energy above the threshold temperature.

Keywords: solid oxide fuel cells (SOFCs); ionic conductivity; raman spectroscopy; powder x-ray diffraction; doped ceria

1. Introduction

Rare earth (RE)-doped ceria systems form one of the most thoroughly studied families of RE oxides for their manifold properties, which make them interesting as catalysts for various processes of CO_2 valorization [1–3], and also as solid electrolytes in solid oxide fuel cells [4–6]. The latter application makes them a valid alternative to the commonly employed Y_2O_3 -stabilized ZrO_2 , as they present high ionic conductivity in the intermediate temperature range (673–973 K), which in principle allows them to lower the cell operating temperature. $\text{Ce}_{0.9}\text{Gd}_{0.1}\text{O}_{1.95}$, for instance, exhibits a remarkable value of $10^{-2} \text{ S cm}^{-1}$ at 773 K [7].

The mechanism of ionic conductivity in doped ceria is quite well known: It occurs thanks to the presence of oxygen vacancies introduced into the structure by partially substituting Ce^{4+} with

a trivalent ion, generally a lanthanide. At sufficiently high temperature, vacancies are provided with energy enough to overcome the activation barrier to diffusion, and are therefore free to move through the lattice. From the crystallographic point of view, the necessary condition for the occurrence of ionic conductivity is the preservation of the CeO_2 fluorite-based structure (hereafter called F), which can be accomplished up to the stability limit of the CeO_2 -based solid solution, i.e., up to a threshold representing the maximum substitution of Ce^{4+} by RE^{3+} which can be tolerated by the CeO_2 structure [8]. Nevertheless, this condition is not sufficient, since the maximum ionic conductivity in doped ceria occurs within the stability region of the CeO_2 -based solid solution at a substitution degree of Ce^{4+} strongly lower than the one corresponding to the aforementioned threshold. The maximum ionic conductivity is observed for instance at $x = 0.1$ [7] and $x = 0.2$ [9,10] in $\text{Ce}_{1-x}\text{Gd}_x\text{O}_{2-x/2}$, and at $x = 0.17$ [11] and $x \sim 0.2$ in $\text{Ce}_{1-x}\text{Sm}_x\text{O}_{2-x/2}$ [12], but the upper compositional limit of the F structure lies at x close to 0.3 in Gd-doped ceria [13,14] and at x ranging between 0.3 and 0.4 [15] or close to 0.3 [16] for Sm-doped ceria. The reason for the described non-coincidence of maximum ionic conductivity and maximum Ce^{4+} substitution is commonly attributed to the formation of $\text{RE}'_{\text{Ce}} : \text{V}_{\text{O}}^{\bullet\bullet}$ aggregates causing phase separation at the nanoscale, where vacancies are trapped at fixed positions, with their movement being consequently hindered [17–21]. The cited aggregates assume the cubic atomic arrangement (hereafter named C) typical of sesquioxides of the smallest rare earths, which is a superstructure of the F structure.

The presence of C nanodomains, responsible for the ionic conductivity reduction observed within the F region, is generally not detectable by average techniques, such as powder x-ray diffraction; on the contrary, they are clearly visible by local techniques, like pair distribution function (PDF) [14,16,22], Transmission Electron Microscopy (TEM) [23,24], and Extended X-ray Absorption Fine Structure (EXAFS) spectroscopy [25–27]. Among these experimental methods, Raman spectroscopy deserves a special mention: Its high sensitivity toward oxygen displacement and, thus, vacancies formation, and its superior ability to clearly distinguish between signals originating from F and C [28,29], make it the technique of choice to be coupled to x-ray diffraction in the experimental investigation of doped ceria [15,30–36].

The study of ionic conductivity in doped ceria is generally limited to lightly doped samples (i.e., up to $x \sim 0.20$ – 0.30 , depending on the specific system); nevertheless, from the viewpoint of basic science, highly doped compositions are of great interest too, as they allow to investigate the effect of $\text{RE}'_{\text{Ce}} : \text{V}_{\text{O}}^{\bullet\bullet}$ aggregates on the reduction/suppression of vacancies migration, and the behavior of the activation barrier as a response to the presence of C domains. In this work, several samples belonging to the $\text{Ce}_{1-x}\text{Gd}_x\text{O}_{2-x/2}$ system with x ranging between 0.30 and 0.50 are studied by means of impedance and micro Raman spectroscopy, and results are compared to data deriving from lightly doped Gd-doped ceria [9] and Sm-doped ceria [12,30]. Compositions located close to the F compositional limit, i.e., with x close to 0.30, exhibit a two-fold behavior of total conductivity and two values of activation energy (E_a), depending on temperature, which suggest the existence of a threshold temperature separating a high from a low temperature conductivity mechanism. In this respect, Raman spectroscopy is of great help by providing information about the trend of Raman shift versus temperature of the F and C phases, and by revealing possible discontinuities which can unravel particular aspects of the conductivity mechanism.

2. Materials and Methods

2.1. Synthesis

Four samples belonging to the $\text{Ce}_{1-x}\text{Gd}_x\text{O}_{2-x/2}$ system having nominal $x = 0.31, 0.34, 0.43,$ and 0.49 were prepared by co-precipitation of the corresponding mixed oxalates, as described in [37,38]. The co-precipitation technique was preferred to other synthetic methods, since it ensures a more intimate mixing of cations with respect for instance to solid state reactions, thus allowing a better homogeneity of the resulting samples [33]. Stoichiometric amounts of Ce (Johnson Matthey ALPHA

99.99% wt.) and Gd_2O_3 were separately dissolved in HCl (13% volume), and the two solutions were subsequently mixed. Oxalates were co-precipitated by adding an oxalic acid solution. Precipitates were filtered, washed, dried overnight, and then treated at 973 K in air for four days to obtain mixed oxides. Samples are named CGO31, CGO34, and so on, according to the Gd atomic percent with respect to the total lanthanide content.

2.2. X-ray Diffraction and Scanning Electron Microscopy—Energy-Dispersive System (SEM-EDS)

Powders of all the obtained mixed oxides were analyzed by x-ray diffraction using a Bragg-Brentano powder diffractometer (Philips PW1050/81, Fe-filtered $\text{Co K}\alpha$ radiation, Amsterdam, The Netherlands); diffraction patterns were collected in the $20\text{--}80^\circ$ angular range, with angular step 0.02° .

The powder morphology, as well as the Gd and Ce amount, and the feature of the sintered pellet surface, were analyzed by scanning electron microscopy coupled to energy-dispersive system (SEM-EDS, Phenom ProX, Phenom World, Eindhoven, The Netherlands).

2.3. Impedance Spectroscopy

Transport properties of all the samples were evaluated by impedance spectroscopy. Powders were pressed by a hydraulic press, and the obtained pellets were sintered in air at 1773 K for 1 h. Plane surfaces of sintered pellets were coated with metallic electrodes by brushing Pt ink (Metalor, Birmingham, UK), which were cured at 1273 K in air. Conductivity was measured by a Frequency Response Analyzer (Iviumstat.h, Ivium Technologies B.V., Eindhoven, The Netherlands) in the 600–1000 K temperature range, 10^{-2} – 10^6 Hz frequency range and under flowing pure O_2 atmosphere. The amplitude of the signal used for the measurements was 30 mV. Data was treated by the equivalent circuits method, as implemented in the Zview software (3.4), consisting in fitting data by a series of one or two ($R_i//Q_i$), depending on the temperature, in series to a resistance R.

2.4. Micro Raman Spectroscopy

High temperature micro Raman analyses were carried out on all the mixed oxides samples employing a Renishaw System 2000 Raman imaging microscope. Specimens were pressed into pellets, and measurements were done at room temperature and at 673, 773, 873, 973, and 1073 K. Raman spectra were obtained by a 633 nm He-Ne laser in the $1000\text{--}100\text{ cm}^{-1}$ range as a result of one accumulation lasting 10 s. At least four different points of each sample were analyzed at room temperatures; afterwards, high temperature spectra were collected on a selected point during both heating and cooling, with a $20\times$ magnification. The laser power was kept at around 2 mW. The wave number has an accuracy of 3 cm^{-1} .

3. Results

3.1. Structural and Morphological Analysis

Figure 1 shows the aspect of powders of samples CGO31 and CGO43 as revealed by scanning electron microscopy. Morphological analyses performed on powders of all samples suggest that the average particles size lies in the range $1\text{--}5\ \mu\text{m}$. Compositional analyses deriving from backscattered electrons reveal that the actual rare earth content is very close to the nominal one.

In Figure 2 SEM microphotographs taken (a) before and (b) after impedance spectroscopy measurements on the surface of sintered pellets of samples CGO43 are presented. Images of all samples show a good compaction degree of the pellet and no appreciable compositional inhomogeneities. Areas with grains having average sizes up to $5\ \mu\text{m}$ are accompanied by much finer grains; this evidence could be most probably attributed to the presence of particles aggregates characterized by lower sinterability than other ones. No effect of impedance spectroscopy measurements was detected on such microstructural features. In Figure 2c the EDS spectrum obtained on a region of CGO43 sample is reported.

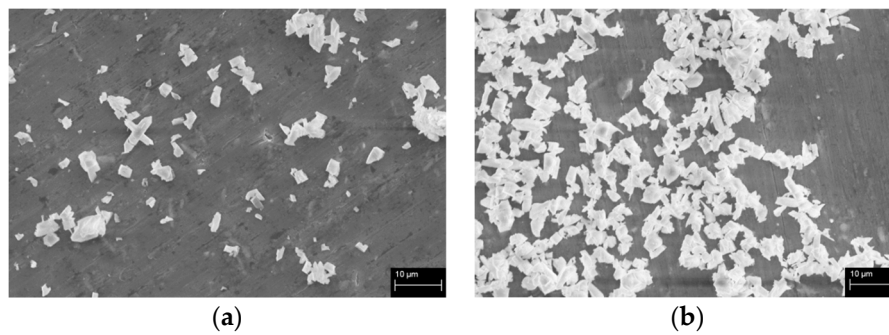


Figure 1. SEM microphotographs taken by secondary electrons on powders of samples (a) CGO31 and (b) CGO43.

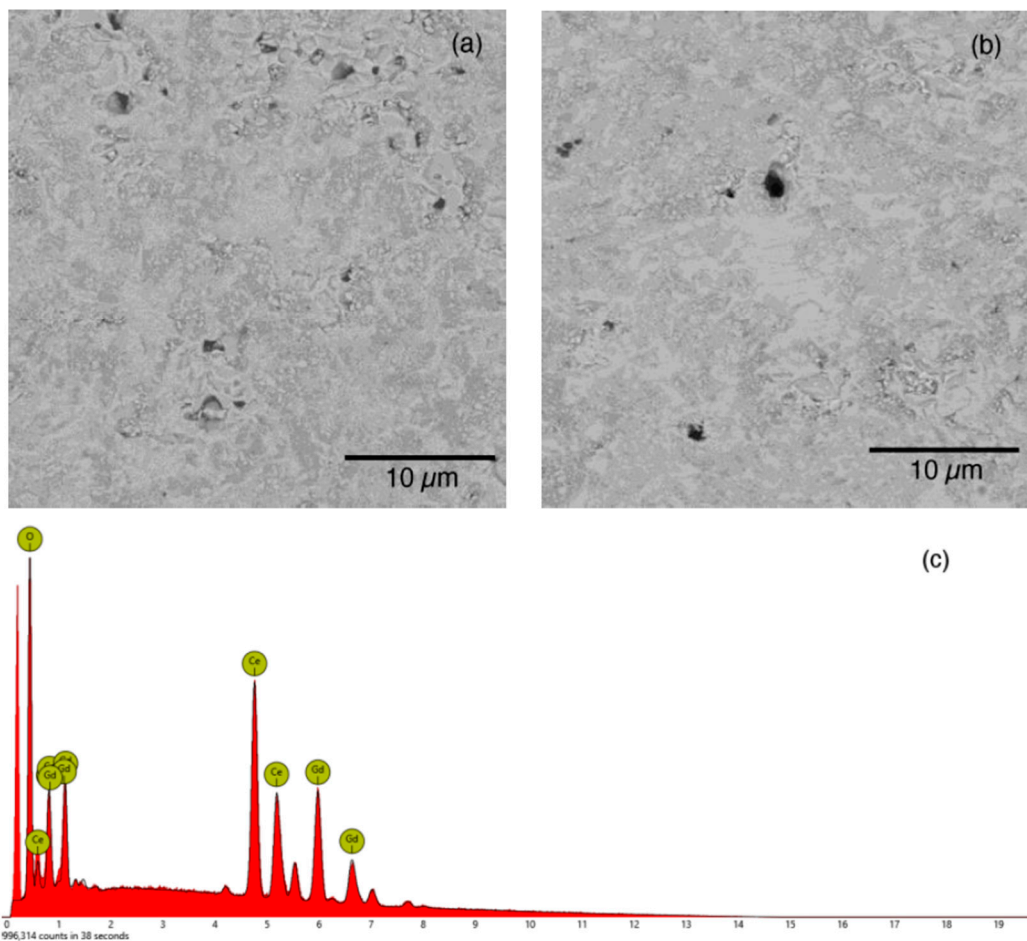


Figure 2. SEM microphotographs taken by back-scattered electrons on the surface of sintered pellets of CGO43 (a) before and (b) after impedance spectroscopy measurements. (c) energy-dispersive system (EDS) spectrum obtained on a region of CGO43 sample.

EDS spectra deriving from different regions reveal that for all samples the actual composition is very close to the nominal one.

All the collected diffraction patterns show only peaks attributable to doped ceria; no hints suggesting the presence of additional phases were detected. In Figure 3 diffractograms of all the samples are reported in a stack. It can be observed that, while sample CGO31 only presents peaks deriving from the F phase, in all the other patterns peaks originating from the C superstructure appear; the intensities of the latter increase with increasing the Gd content. It can also be noticed that peaks common to F and C are perfectly superimposed at each composition. This evidence was widely

discussed in previous papers [13,15,32,39,40] and attributed to the onset of an atomic arrangement having an intermediate character between F and C. This F/C hybrid phase (hereafter called H) can be described as a solid solution where F behaves as a matrix hosting C-structured $Gd'_{Ce} : V_{\ddot{O}}$ domains. C domains, in turn, grow as a finely interlaced phase within F, so that F and C cannot be distinguished at the average scale as two separate phases. Relying on the results of x-ray diffraction analyses, it can be thus concluded that CGO31 lies close to the F/H transition, thus confirming previous data reported in Reference [13].

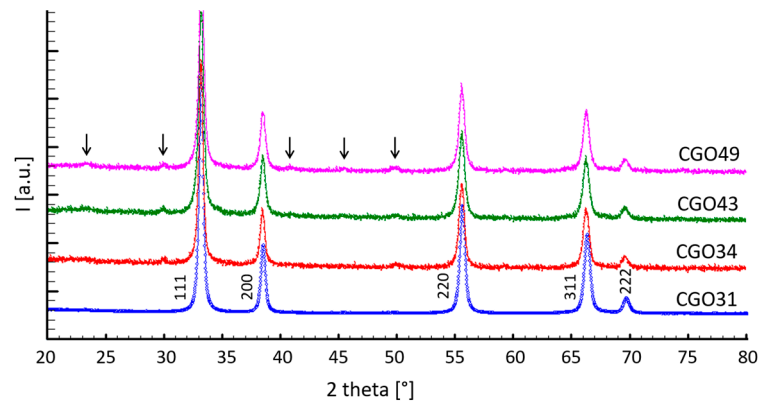


Figure 3. Diffraction patterns of samples CGO31, CGO34, CGO43, and CGO49. In CGO31 Miller indices of the F phase are reported; arrows indicate the position of peaks belonging to the C superstructure.

3.2. Ionic Conductivity

Figure 4 reports the Nyquist plots of impedance spectra obtained (a) at fixed temperature (998 K) for $x = 0.31$ and 0.34 and (b) increasing temperature from 947 K to 998 K for $x = 0.49$. Only one contribution can be recognized given by electrode-related phenomena. The presence of two partially overlapped arcs can be ascribed to some differences between the two Pt electrodes. The total resistance was estimated as the intercepts at high frequency with axis. In particular the total resistance increases with increasing Gd content at fixed temperature and decreases with increasing temperature at fixed Gd content.

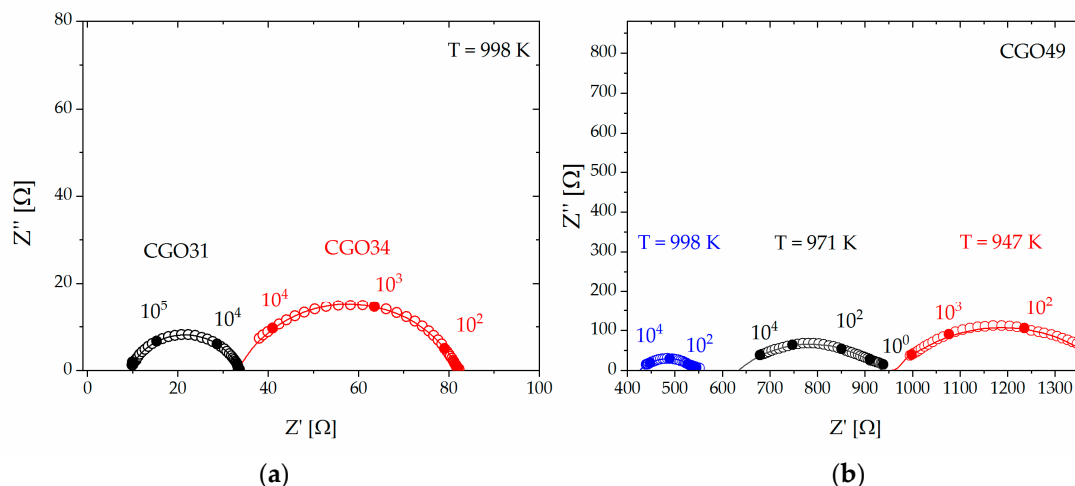


Figure 4. Nyquist plot of impedance spectra of (a) CGO31 and CGO34 samples measured at 998 K and (b) CGO49 sample measured at 998, 971, and 947 K, as reported within panels. Full markers point at frequency decades. Lines represent the best fit of data with model reported in the text.

From total resistance of samples, the conductivity values were calculated and used to evaluate E_a at different temperatures. Arrhenius plots are presented in Figure 5. In the whole temperature

range, conductivity decreases with increasing Gd content, as expected in this compositional range. In addition, a slope change is present for sample CGO31 and, less pronounced, for sample CGO34. Experimental data of each of the two aforementioned samples were in fact fitted by two different regression lines, as evident from Figure 5. The described slope change is due to a variation of E_a taking place around 723–773 K. Such a change is not present in CGO43 and CGO49 samples.

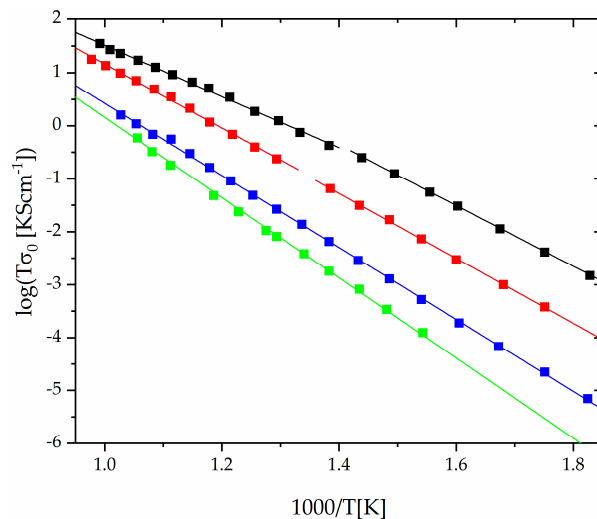


Figure 5. Arrhenius plots of total conductivity of samples CGO31–black, CGO34–red, CGO43–blue, and CGO49–green. Two different regression lines were used to fit data of samples CGO31 and CGO34.

The values of E_a calculated from the above-mentioned slopes are reported in Figure 6. In this plot, previously tested [9] samples with lower Gd content (10 at. % and 20 at. %), are also reported for comparison. Open circles represent unique E_a values, i.e., compositions which do not exhibit slope change in their Arrhenius plot. Solid markers indicate E_a values in the low-temperature (red) or high-temperature (black) regions, in case of slope change.

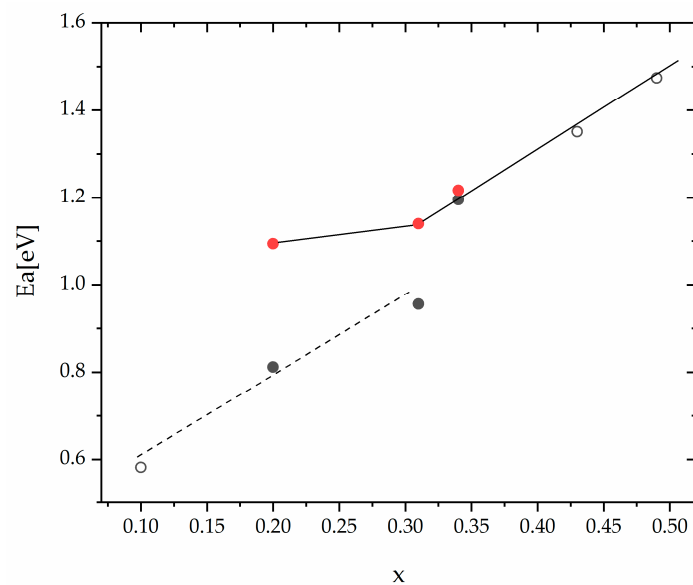


Figure 6. Activation energies of samples CGO31, CGO34, CGO43, and CGO49 as a function of x . Values found for two previously tested [9] samples with lower Gd content (10 at. % and 20 at. %), are also reported. Lines are guides for the eye indicating two series, namely the low-T (solid) and high-T (dashed).

E_a values displayed in Figure 6 can be conveniently divided into two series: The first one grouping low-T values and including samples with $x = 0.43$ and $x = 0.49$ (connected by the solid line); the second one grouping the high-T values and including the sample with $x = 0.10$ (connected by the dashed line).

3.3. Micro Raman Spectroscopy

Raman spectra collected on RE-doped ceria in the F and in the H region present signals attributable to three different structural features: (a) a signal at $\sim 465 \text{ cm}^{-1}$ due to the F_{2g} symmetric vibration mode of the Ce–O bond in eight-fold coordination [29,41], typical of CeO_2 and of CeO_2 -based solid solutions; (b) signals caused by the introduction of the doping cation into F, respectively inducing the creation of vacancies within the Gd coordination sphere [28] (at $\sim 540 \text{ cm}^{-1}$ and $\sim 250 \text{ cm}^{-1}$), and the formation of a REO_8 -type complex not containing oxygen vacancies, due to the partial substitution of Ce by Gd [28] (at $\sim 600 \text{ cm}^{-1}$); and (c) a broad band at $\sim 370 \text{ cm}^{-1}$, to be ascribed to the ($A_g + F_g$) Gd–O symmetrical stretching mode with Gd in six-fold coordination [42], namely the signature of the C structure. With increasing the dopant content, position, intensity, and width of all the cited bands change, as thoroughly discussed in [15,32]: The signal at $\sim 465 \text{ cm}^{-1}$ undergoes first a redshift and, at higher Gd content, a blueshift under the action of the Gd size and of vacancies, respectively; all the other signals increase in intensity and sharpen, since their occurrence is strictly related to the presence of the doping ion.

The effect of rising temperature on Raman spectra of Gd-doped ceria can be appreciated by observing Figure 7, where acquisitions performed on sample CGO34 from 298 K to 1073 K are reported. As generally expected, rising temperature leads to broaden the width and reduce the intensity of all the signals, as a consequence of the increased disorder caused by thermal motion; moreover, all the bands move toward lower Raman shifts, due to the decreasing energy necessary to excite vibrations along progressively looser bonds. The behavior of the main Raman signals of both the F and the C phase as a function of temperature, namely the ones at $\sim 465 \text{ cm}^{-1}$ and $\sim 370 \text{ cm}^{-1}$, respectively, deserve a closer inspection. Figure 8 shows the trend of the aforementioned Raman shifts.

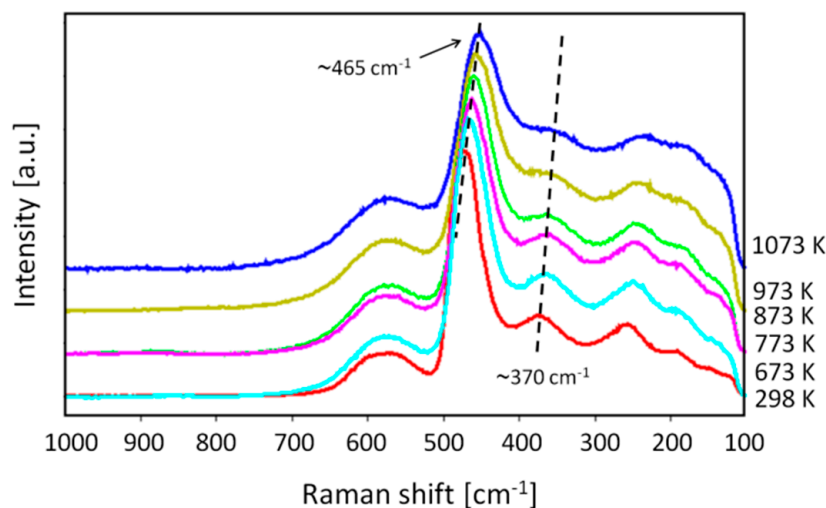


Figure 7. Raman spectra collected on sample CGO34 from 298 K to 1073 K. Dashed lines are a guide for the eye highlighting the movement of Raman shift of the main F ($\sim 465 \text{ cm}^{-1}$) and C ($\sim 370 \text{ cm}^{-1}$) signal toward lower values with increasing temperature.

It can be observed that the trends of both signals show a steeper decrease of the Raman shift above a certain threshold temperature, which is located between 673 K and 773 K, depending on the sample. The slope change occurs for all the samples except CGO49, and it most probably points at an abrupt lengthening and weakening of both the Ce–O and Gd–O bonds (with Ce and Gd in eight- and

six-fold coordination, respectively), thus causing a sudden reduction of the energy needed to excite the vibration along the aforementioned bonds.

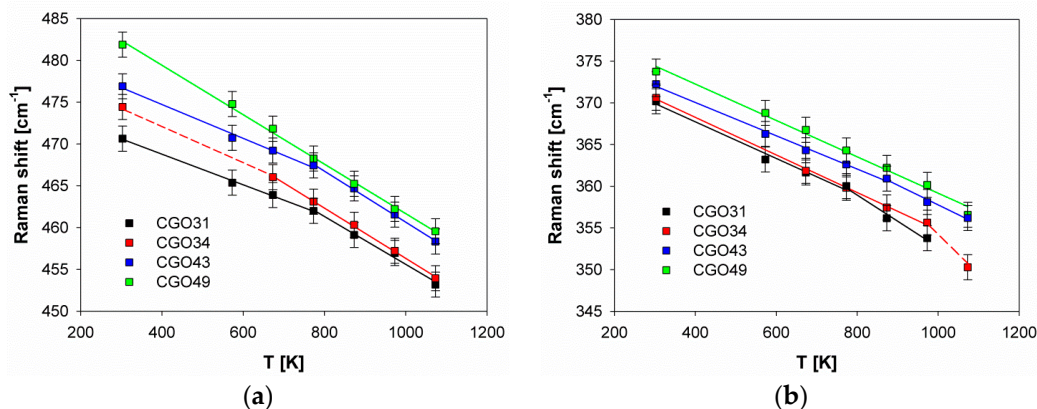


Figure 8. Trend of the Raman shift versus temperature of (a) the F_{2g} vibration mode of Ce–O and (b) the $(A_g + F_g)$ Gd–O stretching mode. Dashed lines are a guide for the eye, while solid lines are regression lines.

4. Discussion

Based on the results of impedance spectroscopy measurements, three different conductivity mechanisms can be recognized in the 0.1–0.5 x range.

(1) $0.10 \leq x < 0.20$. In this range a unique E_a value of 0.6–0.8 eV is observed through the whole temperature span. Bulk E_a is considered to be the sum of two contributions, namely the migration enthalpy (H_m) and the association enthalpy (H_a), with the former being the energy needed to induce the hopping of vacancies through the lattice, and the latter the energy needed to force vacancies out of the C-based aggregates [43]. According to Inaba and Tagawa [44], while H_a increases with increasing the dopant amount due to the growing stability of progressively larger C domains, H_m remains essentially constant, assuming the value of around 0.60 eV. In the light of these considerations, it can be deduced that for $x = 0.10$ vacancies are randomly dispersed within the F matrix and essentially free to move through the lattice; this conclusion is in good agreement with the results of numerous studies, claiming that this is the region which provides the maximum ionic conductivity [7,9,10]. C nanodomains, existing in an embryonic form even for $x = 0.125$ as revealed by the pair distribution function technique [14], are not able to significantly affect ionic conductivity.

(2) $0.20 \leq x \leq 0.34$. In this compositional interval a two-fold behavior is observed: At temperature lower than ~ 723 K an E_a of ~ 1.1 eV is found, while above the value is approximately 0.8–0.9 eV. The cited temperature can be thus considered as a threshold: Below it, a low temperature behavior occurs, where vacancies, being trapped within C microdomains, are characterized by a reduced mobility, and therefore by a high E_a . This interpretation is fully compatible with the results of several local techniques, such as Raman spectroscopy [15,32], EXAFS [25,26], TEM [23,24], and PDF [14], which agree about the existence of C microdomains. The described scenario is also in good agreement with the drop in conductivity observed even within the F region at $x > 0.1$ [7] or 0.2 [9,10]. Above the threshold temperature, on the contrary, vacancies are mainly free to move through the lattice, and E_a is similar to the one observed in the 0.1–0.2 x range. It is noteworthy that for $x = 0.34$ the low temperature activation energies are still distinguishable but very close to the high temperature one, meaning that with increasing x even above the threshold temperature a significant part of C microdomains survives.

Raman spectra collected on samples CGO31 and CGO34 support the conclusions driven from the results of impedance spectroscopy, suggesting that above the threshold temperature both the release and the mobility of vacancies are enhanced. The slope change observable above ~ 750 K in the trend of Raman shift versus temperature of the C phase (see Figure 8b) can be ascribed to an abrupt lengthening and weakening of the Gd–O bond, responsible for facilitating the dissociation of the

C-structured aggregates and hence for promoting the release of oxygen vacancies. This interpretation is in good agreement with the strong reduction of H_a found above the threshold temperature. A similar discontinuity, also revealed in the Raman shift of the F structure (see Figure 8a), points at a lengthening even of the Ce–O bond. This phenomenon acts in the same direction as the lengthening of the Gd–O distance within C microdomains, as it weakens the bond and fosters its rupture, thus enhancing the mobility of vacancies through F.

(3) $0.43 \leq x \leq 0.49$. In this region ionic conductivity is again ruled by just one E_a , whose value is remarkably higher than in the 0.10–0.20 x region (1.3–1.5 eV with respect to 0.6–0.8 eV); moreover, data are well aligned with the higher value of samples, with x ranging between 0.20 and 0.34, so that all the cited experimental points can be conveniently fitted by a regression line. The described scenario suggests that on average vacancies are blocked within C microdomains. Moreover, the increasing trend of E_a with x is compatible with the corresponding increasing size of C microdomains [16,45], which makes them progressively more stable, consequently enhancing the energy amount needed to release a vacancy from the defect aggregate. Correspondingly, the trend of the Raman shifts related to the main signal of both C and F of CGO49 do not show any slope change as a function of temperature.

5. Conclusions

Ionic conductivity and high temperature Raman features of several samples of heavily Gd-doped ceria ($\text{Ce}_{1-x}\text{Gd}_x\text{O}_{2-x/2}$ with $x = 0.31, 0.34, 0.43,$ and 0.49) were investigated and compared to data deriving from samples with $x = 0.10$ and 0.20 . Aim of the study was to identify mechanisms lying behind the transport of the oxygen ion in the 600–1000 K temperature range. Three different behaviors were identified, namely: (a) in the $0.10 \leq x < 0.20$ range just one E_a appears. Its value (0.6–0.8 eV) is compatible with a random dispersion of vacancies within the CeO_2 -based solid solution; consequently, vacancies are free to move through the lattice. (b) in the $0.20 \leq x \leq 0.34$ range two activation energies occur, giving rise to a threshold temperature (~ 723 K), below which vacancies are mainly trapped within defect aggregates, and above which they are free to move. This interpretation is fully confirmed by results of Raman spectroscopy, which demonstrate the existence of the aforementioned threshold temperature even in the trend of the Raman shift versus temperature of the main signals related both to the CeO_2 -based solid solution and to the C-structured defect aggregates. (c) in the $0.43 \leq x \leq 0.49$ range a unique E_a , higher than in the $0.10 \leq x < 0.20$ interval, suggests that vacancies are mainly blocked within defect aggregates at each temperature considered.

Author Contributions: Conceptualization, C.A., S.P., S.M., M.P., M.M.C. and M.V.; methodology, C.A., S.P., M.P. and M.V.; validation, S.P. and S.M.; formal analysis, S.P. and S.M.; investigation, C.A., S.P., S.M., M.P., M.M.C. and M.V.; writing—original draft preparation, C.A.; writing—review and editing, C.A., S.P., S.M., M.P., M.M.C. and M.V.; visualization, S.P., S.M.; supervision, M.V.

Funding: This research received no external funding.

Conflicts of Interest: The authors declare no conflict of interest.

References

1. Boaro, M.; Colussi, S.; Trovarelli, A. Ceria-based materials in hydrogenation and reforming reactions for CO_2 valorization. *Front. Chem.* **2019**, *7*, 28. [[CrossRef](#)] [[PubMed](#)]
2. Le Saché, E.; Johnson, S.; Pastor-Pérez, L.; Horri, B.A.; Reina, T.R. Biogas upgrading via dry reforming over a Ni-Sn/ CeO_2 - Al_2O_3 catalyst: Influence of the biogas source. *Energies* **2019**, *12*, 1007. [[CrossRef](#)]
3. Smith, P.J.; Smith, L.; Dummer, N.F.; Douthwaite, M.; Willock, D.J.; Howard, M.; Knight, D.W.; Taylor, S.H.; Hutchings, G.J. Investigating the Influence of Reaction Conditions and the Properties of Ceria for the Valorisation of Glycerol. *Energies* **2019**, *12*, 1359. [[CrossRef](#)]
4. Skinner, S.J.; Kilner, J.A. Oxygen ion conductors. *Mater. Today* **2003**, *6*, 30–37. [[CrossRef](#)]
5. Jaiswal, N.; Tanwar, K.; Suman, R.; Kumar, D.; Upadhyay, S.; Parkash, O. A brief review on ceria based solid electrolytes for solid oxide fuel cells. *J. Alloys Compd.* **2019**, *781*, 984–1005. [[CrossRef](#)]

6. Presto, S.; Barbucci, A.; Viviani, M.; Ilhan, Z.; Ansar, A.; Soysal, D.; Thorel, A.S.; Abreu, J.; Chesnaud, A.; Politova, T.; et al. IDEAL-Cell, Innovative Dual mEmbrAne fuel-Cell: Fabrication and Electrochemical Testing of First Prototypes. *ECS Trans.* **2009**, *25*, 773–782.
7. Steele, B.C.H. Appraisal of Ce_{1-x}Gd_yO_{2-y/2} electrolytes for IT-SOFC operation at 500 °C. *Solid State Ion.* **2000**, *129*, 95–110. [[CrossRef](#)]
8. Artini, C. RE-doped ceria systems and their performance as solid electrolytes: A puzzling tangle of structural issues at the average and local scale. *Inorg. Chem.* **2018**, *57*, 13047–13062. [[CrossRef](#)]
9. Artini, C.; Pani, M.; Lausi, A.; Masini, R.; Costa, G.A. High temperature structural study of Gd-doped ceria by synchrotron X-ray diffraction (673 K ≤ T ≤ 1073 K). *Inorg. Chem.* **2014**, *53*, 10140–10149. [[CrossRef](#)]
10. Tianshu, Z.; Hing, P.; Huang, H.; Kilner, J. Ionic conductivity in the CeO₂–Gd₂O₃ system (0.05 ≤ Gd/Ce ≤ 0.4) prepared by oxalate coprecipitation. *Solid State Ion.* **2002**, *148*, 567–573. [[CrossRef](#)]
11. Aygün, B.; Özdemir, H.; Faruk Öksüzömer, M.A. Structural, morphological and conductivity properties of samaria doped ceria (Sm_xCe_{1-x}O_{2-x/2}) electrolytes synthesized by electrospinning method. *Mater. Chem. Phys.* **2019**, *232*, 82–87. [[CrossRef](#)]
12. Artini, C.; Carnasciali, M.M.; Viviani, M.; Presto, S.; Plaisier, J.R.; Costa, G.A.; Pani, M. Structural properties of Sm-doped ceria electrolytes at the fuel cell operating temperatures. *Solid State Ion.* **2018**, *315*, 85–91. [[CrossRef](#)]
13. Artini, C.; Costa, G.A.; Pani, M.; Lausi, A.; Plaisier, J. Structural characterization of the CeO₂/Gd₂O₃ mixed system by synchrotron X-ray diffraction. *J. Solid State Chem.* **2012**, *190*, 24–28. [[CrossRef](#)]
14. Scavini, M.; Coduri, M.; Allieta, M.; Brunelli, M.; Ferrero, C. Probing complex disorder in Ce_{1-x}Gd_xO_{2-x/2} using the pair distribution function analysis. *Chem. Mater.* **2012**, *24*, 1338–1345. [[CrossRef](#)]
15. Artini, C.; Pani, M.; Carnasciali, M.M.; Buscaglia, M.T.; Plaisier, J.; Costa, G.A. Structural features of Sm- and Gd-doped ceria studied by synchrotron X-ray diffraction and μ -Raman spectroscopy. *Inorg. Chem.* **2015**, *54*, 4126–4137. [[CrossRef](#)]
16. Coduri, M.; Masala, P.; Allieta, M.; Peral, I.; Brunelli, M.; Biffi, C.A.; Scavini, M. Phase transformations in the CeO₂-Sm₂O₃ system: A multiscale powder diffraction investigation. *Inorg. Chem.* **2018**, *57*, 879–891. [[CrossRef](#)]
17. Minervini, L.; Zacate, M.O.; Grimes, R.W. Defect cluster formation in M₂O₃-doped CeO₂. *Solid State Ion.* **1999**, *116*, 339–349. [[CrossRef](#)]
18. Acharya, S.A.; Gaikwad, V.M.; Sathe, V.; Kulkarni, S.K. Influence of gadolinium doping on the structure and defects of ceria under fuel cell operating temperature. *Appl. Phys. Lett.* **2014**, *104*, 113508. [[CrossRef](#)]
19. Inaba, H.; Sagawa, R.; Hayashi, H.; Kawamura, K. Molecular dynamics simulation of gadolinia-doped ceria. *Solid State Ion.* **1999**, *122*, 95–103. [[CrossRef](#)]
20. Ye, F.; Mori, T.; Ou, D.R.; Zou, J.; Auchterlonie, G.; Drennan, J. Compositional and structural characteristics of nano-sized domains in gadolinia-doped ceria. *Solid State Ion.* **2008**, *179*, 827–831. [[CrossRef](#)]
21. Wang, B.; Lewis, R.J.; Cormack, A.N. Computer simulations of large-scale defect clustering and nanodomain structure in gadolinia-doped ceria. *Acta Mater.* **2011**, *59*, 2035–2045. [[CrossRef](#)]
22. Coduri, M.; Scavini, M.; Pani, M.; Carnasciali, M.M.; Klein, H.; Artini, C. From nano to microcrystals: Effect of different synthetic pathways on defects architecture in heavily Gd-doped ceria. *Phys. Chem. Chem. Phys.* **2017**, *19*, 11612–11630. [[CrossRef](#)] [[PubMed](#)]
23. Ye, F.; Mori, T.; Ou, D.R.; Zou, J.; Drennan, J. A structure model of nano-sized domain in Gd-doped ceria. *Solid State Ion.* **2009**, *180*, 1414–1420. [[CrossRef](#)]
24. Ou, D.R.; Mori, T.; Ye, F.; Zou, J.; Auchterlonie, G.; Drennan, J. Oxygen-vacancy ordering in lanthanide-doped ceria: Dopant-type dependence and structure model. *Phys. Rev. B* **2008**, *77*, 024108. [[CrossRef](#)]
25. Deguchi, H.; Yoshida, H.; Inagaki, T.; Horiuchi, M. EXAFS study of doped ceria using multiple data set fit. *Solid State Ion.* **2005**, *176*, 1817–1825. [[CrossRef](#)]
26. Kossov, A.; Wang, Q.; Korobko, R.; Grover, V.; Feldman, Y.; Wachtel, E.; Tyagi, A.K.; Frenkel, A.I.; Lubomirsky, I. Evolution of the local structure at the phase transition in CeO₂-Gd₂O₃ solid solutions. *Phys. Rev. B* **2013**, *87*, 054101. [[CrossRef](#)]
27. Nitani, H.; Nakagawa, T.; Yamanouchi, M.; Osuki, T.; Yuya, M.; Yamamoto, T.A. XAFS and XRD study of ceria doped with Pr, Nd or Sm. *Mater. Lett.* **2004**, *58*, 2076–2081. [[CrossRef](#)]
28. Nakajima, A.; Yoshihara, A.; Ishigame, M. Defect-induced Raman spectra in doped CeO₂. *Phys. Rev. B* **1994**, *50*, 13297–13307. [[CrossRef](#)]

29. McBride, J.R.; Hass, K.C.; Pointdexter, B.D.; Weber, W.H. Raman and X-ray studies of Ce_{1-x}RE_xO_{2-y}, where RE=La, Pr, Nd, Eu, Gd, and Tb. *J. Appl. Phys.* **1994**, *76*, 2435–2441. [[CrossRef](#)]
30. Presto, S.; Artini, C.; Pani, M.; Carnasciali, M.M.; Massardo, S.; Viviani, M. Ionic conductivity and local structural features in Ce_{1-x}Sm_xO_{2-x/2}. *Phys. Chem. Chem. Phys.* **2018**, *20*, 28338–28345. [[CrossRef](#)]
31. Artini, C.; Carnasciali, M.M.; Costa, G.A.; Plaisier, J.R.; Pani, M. A novel method for the evaluation of the Rare Earth (RE) coordination number in RE-doped ceria through Raman spectroscopy. *Solid State Ion.* **2017**, *311*, 90–97. [[CrossRef](#)]
32. Artini, C.; Pani, M.; Carnasciali, M.M.; Plaisier, J.R.; Costa, G.A. Lu-, Sm- and Gd-doped ceria: A comparative approach to their structural properties. *Inorg. Chem.* **2016**, *55*, 10567–10579. [[CrossRef](#)] [[PubMed](#)]
33. Horlait, D.; Claparède, L.; Clavier, N.; Szencnekt, S.; Dacheux, N.; Ravaux, J.; Podor, R. Stability and structural evolution of CeIV_{1-x}LnIII_xO_{2-x/2} solid solutions: A coupled μ -Raman/XRD approach. *Inorg. Chem.* **2011**, *50*, 150–161. [[CrossRef](#)] [[PubMed](#)]
34. Mandal, B.P.; Roy, M.; Grover, V.; Tyagi, A.K. X-ray diffraction, μ -Raman spectroscopic studies on CeO₂-RE₂O₃ (RE=Ho, Er) systems: Observation of parasitic phases. *J. Appl. Phys.* **2008**, *103*, 033506. [[CrossRef](#)]
35. Mandal, B.P.; Grover, V.; Roy, M.; Tyagi, A.K. X-ray diffraction and Raman spectroscopic investigation on the phase relations in Yb₂O₃- and Tm₂O₃-substituted CeO₂. *J. Am. Ceram. Soc.* **2007**, *90*, 2961–2965. [[CrossRef](#)]
36. Grover, V.; Banerji, A.; Sengupta, P.; Tyagi, A.K. Raman, XRD and microscopic investigations on CeO₂-Lu₂O₃ and CeO₂-Sc₂O₃ systems: A sub-solidus phase evolution study. *J. Solid State Chem.* **2008**, *181*, 1930–1935. [[CrossRef](#)]
37. Artini, C.; Costa, G.A.; Carnasciali, M.M.; Masini, R. Stability fields and structural properties of intra rare earths perovskites. *J. Alloys Compd.* **2010**, *494*, 336–339. [[CrossRef](#)]
38. Artini, C.; Costa, G.A.; Masini, R. Study of the formation temperature of mixed LaREO₃ (RE≡Dy, Ho, Er, Tm, Yb, Lu) and NdGdO₃ oxides. *J. Therm. Anal. Calorim.* **2011**, *103*, 17–21. [[CrossRef](#)]
39. Artini, C.; Gigli, L.; Carnasciali, M.M.; Pani, M. Structural properties of the (Nd,Dy)-doped ceria system by synchrotron X-ray diffraction. *Inorganics* **2019**, *7*, 94. [[CrossRef](#)]
40. Artini, C.; Nelli, I.; Pani, M.; Costa, G.A.; Caratto, V.; Locardi, F. Thermal decomposition of Ce-Sm and Ce-Lu mixed oxalates: Influence of the Sm- and Lu-doped ceria structure. *Thermochim. Acta* **2017**, *651*, 100–107. [[CrossRef](#)]
41. Weber, W.H.; Hass, K.C.; Mc Bride, J.R. Raman study of CeO₂: Second-order scattering, lattice dynamics, and particle-size effects. *Phys. Rev. B* **1993**, *48*, 178–185. [[CrossRef](#)] [[PubMed](#)]
42. Ubaldini, A.; Carnasciali, M.M. Raman characterisation of powder of cubic RE₂O₃ (RE = Nd, Gd, Dy, Tm, and Lu), Sc₂O₃ and Y₂O₃. *J. Alloys Compd.* **2008**, *454*, 374–378. [[CrossRef](#)]
43. Avila-Paredes, H.-J.; Shvareva, T.; Chen, W.; Navrotsky, A.; Kim, S. A correlation between the ionic conductivities and the formation enthalpies of trivalent-doped ceria at relatively low temperatures. *Phys. Chem. Chem. Phys.* **2009**, *11*, 8580–8585. [[CrossRef](#)] [[PubMed](#)]
44. Inaba, H.; Tagawa, H. Ceria-based solid electrolytes. *Solid State Ion.* **1996**, *83*, 1–16. [[CrossRef](#)]
45. Coduri, M.; Scavini, M.; Allieta, M.; Brunelli, M.; Ferrero, C. Defect structure of Y-doped ceria on different length scales. *Chem. Mater.* **2013**, *25*, 4278–4289. [[CrossRef](#)]

